



HAL
open science

Climatology in shallow caves with negligible ventilation: Heat and mass transfer

Beatrice Guerrier, Frédéric Doumenc, Aymeric Roux, Sophie Mergui,
Pierre-Yves Jeannin

► **To cite this version:**

Beatrice Guerrier, Frédéric Doumenc, Aymeric Roux, Sophie Mergui, Pierre-Yves Jeannin. Climatology in shallow caves with negligible ventilation: Heat and mass transfer. International Journal of Thermal Sciences, 2019, 146, pp.106066. 10.1016/j.ijthermalsci.2019.106066 . hal-02289214

HAL Id: hal-02289214

<https://hal.science/hal-02289214>

Submitted on 18 Sep 2019

HAL is a multi-disciplinary open access archive for the deposit and dissemination of scientific research documents, whether they are published or not. The documents may come from teaching and research institutions in France or abroad, or from public or private research centers.

L'archive ouverte pluridisciplinaire **HAL**, est destinée au dépôt et à la diffusion de documents scientifiques de niveau recherche, publiés ou non, émanant des établissements d'enseignement et de recherche français ou étrangers, des laboratoires publics ou privés.

Climatology in shallow caves with negligible ventilation: heat and mass transfer

Béatrice Guerrier^{a,*}, Frédéric Doumenc^{a,b}, Aymeric Roux^a, Sophie Mergui^{a,b}, Pierre-Yves Jeannin^c

^a*Laboratoire FAST, Univ. Paris-Sud, CNRS, Université Paris-Saclay,
F-91405, Orsay, France*

^b*Sorbonne Université, UFR 919, 4 place Jussieu,
F-75252, Paris Cedex05, France*

^c*Swiss Institute for Speleology and Karstology (SISKA),
CH-2301, La Chaux-de-Fonds, Switzerland*

Abstract

The present numerical study investigates the effect of a cavity located at shallow depth below ground surface. The temperature field in the rock matrix surrounding the cave is significantly deformed compared to the case without cavity. Fluxes at cave wall, related to radiation, air-convection and evaporation/condensation (in case of a humid cave), all contribute to a significant homogenization of wall temperatures. In case of high humidity, simulations of evaporation/condensation periods show that some parts of the wall may be durably (several months) subjected to significant condensation (or evaporation). Real meteorological data, i.e. 77 years of external temperature data of the Gourdon station in France, have been used as input of the model. Results of simulations have been compared to experimental temperature of Lascaux cave, with good agreement considering some simplifying hypotheses assumed for this modeling. The asset of such a model is the low computing time required to simulate several years, and thus its ability to follow long time evolution. Results significantly improve our understanding of conditions taking place in a shallow cavity, what will help improving the management of caves, especially those with very fragile decorations such as Paleolithic paintings. The model may help to identify areas which are the most exposed to weathering and to test the effect of past and potential changes in nearby conditions. It may also be useful for managing shallow underground constructions (e.g. a mine or even a cellar).

Keywords: cave - karstic massif - temperature - humidity - heat transfer - condensation -

*Corresponding author, guerrier@fast.u-psud.fr, FAST, Bât. Pascal (n°530), Campus Universitaire, 91405 Orsay, France

1. Introduction

Caves represent fragile ecosystems where biogeochemical processes largely depend on cave temperature and humidity. Caves also host unique environmental records and paleolithic wall-paintings whose conservation closely depends on cave climate as well. Yet little is known about the relative importance of individual mechanisms transferring heat from the surface to the cave environment. Achieving a good understanding of the thermal response of caves to climate change or to perturbations is central to protect cave painting [1, 2, 3, 4] and organisms living in karst [5, 6, 7], as well as to interpret paleoenvironmental indicators recorded in speleothems such as dissolution/precipitation rates [8, 9], and geochemical partitioning [10].

Temperature and humidity variations are usually very little in caves [5, 11, 12]. This very stable environment strongly slows down weathering processes. This explains why wall paintings could be preserved through many thousands of years (e.g. 18 000 years in the case of Lascaux cave). The absence of rain, frost, sun and temperature change strongly reduces the number and the effect of processes able to damage the wall surface [13, 14, 15].

Temperature on Earth surface is known to change with daily, seasonal, decadal and longer cycles. The amplitude of these variations decreases with depth depending on their time scale [16]. Depending on the rock diffusivity, daily variations are smoothed away to 99% at about one meter depth, yearly cycles at about 15 meters, and longer variations propagate deeper (e.g. [17, 18]). Data from boreholes from all over the world confirm that in most cases temperature smoothing with depth behaves according to heat conduction through a more or less homogeneous medium (bedrock). The overall temperature gradient depends on the intensity of the heat flux and on the value of the rock heat conductivity [19]. In the near surface (~ 10 m) the rock temperature is mainly controlled by the outside temperature, which varies considerably along the year. Therefore, in this zone the temperature gradient varies with the season and the depth. Close to the surface, its maximum value is a few degrees per meter and it changes sign between winter and summer. The zone with annual temperature variations larger than $\sim 5\%$ of the outside temperature variation is often called "heterothermic zone" [20]. The deeper part of the massif, with a stable temperature all along the year, is called "homothermic zone" by the same author.

The present paper focusses on heat transfer in a karst massif including caves or cavities located

30 within the heterothermic zone, also sometimes labelled as "shallow caves". As an illustration, we use
31 a geometry which partially mimics the entrance part (Hall of Bulls) of the Lascaux cave in France.
32 This cave is almost not ventilated and belongs to "confined cave" according to the definition given
33 by Bourges et al. [12]. De Freitas and co-authors [21, 22, 23] also studied climate of a shallow cave,
34 but conversely to Lascaux, Glowworm Cave is strongly ventilated.

35 Shallow caves, but also mines or tunnels are voids cutting across the rock medium. With a
36 size of several meters they create a disruption in the conductive medium (bedrock). Therefore,
37 temperature along their respective walls is not uniform inducing heat exchanges within the cavity.
38 Air humidity in underground voids is usually close to vapor saturation. This is at least the case
39 in caves with a reduced air exchange with the outside atmosphere, such as Lascaux cave [24]. In
40 this situation any change in temperature may produce condensation or evaporation at the cave
41 wall. This specific environment (wall with condensation water) seems to enhance the development
42 of bacterial or fungic mats [25], which in turn can produce weathering of the wall surface.

43 The aim of the present study is to assess the shape and evolution of the temperature field
44 produced by a void within the heterothermic zone, and to assess heat exchanges inside the cavity in
45 order to evaluate the position, seasonality and quantity of condensation/evaporation taking place at
46 cave walls. The study example is based on data from Lascaux cave but provides indications about
47 processes taking place in any cave, mines or tunnels located at shallow depth (less than about
48 15 meters below ground). Conditions in this environment are important for the preservation of
49 Paleolithic painted caves, but it provides also an interesting base for understanding habitats in this
50 part of the critical zone [26], as well as for interpreting paleoclimatic records from speleothemes.

51 Since the purpose of this study is to highlight the general trends that characterize the thermal
52 behavior of shallow caves, the conceptual model used in the following keeps only the main charac-
53 teristics of the configuration of such caves and uses some simplifying assumptions. Concerning the
54 rock matrix surrounding the cavity, heat is assumed to be transferred only by conduction through
55 a homogeneous rock. Advection due to air or water flows is assumed to be negligible. In the case
56 studied here the cave is assumed to be sufficiently far from other similar caves.

57 Temperature at ground surface is given by air temperature and is assumed uniform, i.e. we do
58 not take into account spatial variations due for instance to different expositions to solar insolation.

59 Concerning the overall heat flux from the bottom of the karst aquifer, measurements in many
60 karst massifs showed that the flux of water at the bottom of the karst aquifer is usually high enough

61 to drain away most of the geothermal heat. Observed gradients typically range between 0.23 and
62 0.6°C per 100 meters [27, 28, 29]. This gradient (and corresponding flux) is low compared to the
63 usual geothermal gradient of $\sim 3^\circ\text{C}/100\text{m}$. Thus most of the simulations are performed under the
64 assumption of zero flux at the bottom of the karst aquifer. Some simulations using a geothermal
65 gradient of $\sim 3^\circ\text{C}/100\text{m}$ are also performed in order to estimate the influence of such a gradient
66 on the thermal behavior of the cavity.

67 Finally the cave is assumed to be "confined", i.e. without any significant exchange of air with
68 the outside atmosphere. In Lascaux cave, the presence of two succeeding air-locks at the cave
69 entrance, as well as measurements of cave and outside atmosphere (temperature, pressure) made
70 by Schoeller [30], Vouvé et al. [31], and Malaurent et al. [24] show that some exchange still takes
71 place, but are rather low.

72 Temperature variations in Lascaux cave are small (less than 1°C) and differences between air
73 and rock temperature even smaller ($\sim 0.1^\circ\text{C}$). Air humidity measured in the cave always ranges
74 between 98 and 100% [31]. In these conditions all fluxes are small and smooth, meaning that small
75 temperature differences may shift conditions from evaporation to condensation or the opposite.

76 Inside the cavity, processes considered in the physical model are convection of air within the
77 cave volume, heat radiation between facing walls and evapo-condensation at cave walls. In order
78 to limit the complexity of the model and to get "reasonable" computing time for simulations over
79 long periods (several decades), the model is 2D and the description of convection is simplified.

80 The paper is organised as follows: the geometry, physical model, thermophysical properties and
81 numerical method used for the simulations are described first. Then the thermal response of the
82 cavity to a periodic yearly variation of the external temperature is considered. The perturbation
83 induced by the cavity in the massif, the relative weight of the different heat transfer modes in
84 the cavity and the evaporation/condensation phases are deduced from the analysis of this periodic
85 regime. Finally real meteorologic data (77 years) of the external temperature are used as input
86 of the model and simulation results are compared to experimental data collected in Lascaux cave.
87 Some suggestions to go further in the representation of such shallow cavities are drawn in the
88 conclusion.

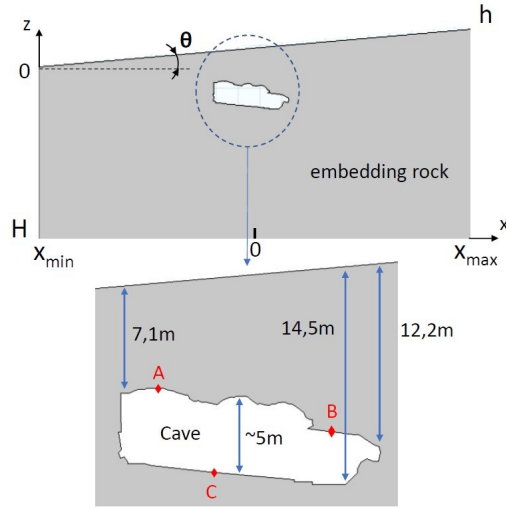


Figure 1: Top: computational model $\mathcal{D} = \mathcal{C} \cup \mathcal{M}$, including the cavity \mathcal{C} and the surrounding karst massif \mathcal{M} . Bottom: zoom on the cavity, with the position of the three fictive sensors A, B and C.

89 2. Modeling

90 2.1. Domain geometry

91 We consider a cave embedded in a karst massif. The geometry, inclination and location of the
 92 cavity in the massif partially mimics the entrance passage of the Lascaux cave in France. Figure 1
 93 shows the computational domain \mathcal{D} that includes the karst massif \mathcal{M} and the cave \mathcal{C} . For the sake
 94 of simplicity, the geometry is 2D. The cave is closed, i.e. there is no mass transfer between the cave
 95 and the surroundings.

96 The size of the computational domain \mathcal{D} is $H = -40\text{ m}$, $h = 8.75\text{ m}$, $x_{\min} = -51\text{ m}$, $x_{\max} =$
 97 49 m . The tilt of the upper surface, θ , is 5° . The vertical distance d_v from the cave to the external
 98 ground surface is close to 7 m and 14.5 m for the highest and lowest points, respectively (cf. Figure
 99 1, with $d_v = -z + (x - x_{\min}) \tan \theta$). The height inside the cave is about 5 m in most of the cavity.
 100 The cross-section of the cavity is 74.6 m^2 (i.e. volume per unit length in the transverse direction)
 101 and the perimeter is 44.3 m .

102 Three fictive "sensors" located in the upper or lower part of the ceiling and on the floor will be
 103 used in the following to analyze the results (cf. red symbols in Figure 1). Their coordinates $(x; z)$
 104 are $(-8.19\text{ m}; -3.30\text{ m})$ for A sensor, $(3.40\text{ m}; -6.15\text{ m})$ for B sensor, and $(-3.92\text{ m}; -8.85\text{ m})$ for C
 105 sensor. The respective depths d_v are 7.05 m , 10.91 m and 12.97 m for A , B and C sensors.

106 *2.2. Karst massif*

107 Assuming that heat transfer is mainly conductive in the embedding rock with a constant diffu-
 108 sivity (homogeneous rock), the temperature at each point inside the domain \mathcal{M} satisfies the heat
 109 equation

$$\frac{\partial T}{\partial t} = a_r \left(\frac{\partial^2 T}{\partial x^2} + \frac{\partial^2 T}{\partial z^2} \right), \quad (1)$$

110 where $T(x, z, t)$ is the local temperature in \mathcal{M} , x and z are the horizontal and vertical coordinates,
 111 respectively, and a_r is the rock diffusivity ($\text{m}^2 \cdot \text{s}^{-1}$).

112 The external boundary conditions for the sub-domain \mathcal{M} are the followings:

- 113 • Lateral boundary conditions: the computational domain \mathcal{D} being much larger than the size
 114 of the cave, the perturbation resulting from the presence of the shallow cavity is negligible at
 115 the lateral boundaries of the domain and the flux is set to zero:

$$\frac{\partial T}{\partial x} \Big|_{x=x_{min}} = \frac{\partial T}{\partial x} \Big|_{x=x_{max}} = 0. \quad (2)$$

- 116 • Top boundary condition: at the external ground surface, the temperature is imposed (Dirichlet
 117 condition)

$$T(x, z, t) = T_{ex}(t) \quad \text{for } x_{min} < x < x_{max} \quad \text{and } z = (x - x_{min}) \tan \theta, \quad (3)$$

118 where $T_{ex}(t)$ is the time varying outside temperature. We use in the following a periodic
 119 variation with a yearly period or real meteorological data.

- 120 • Bottom boundary condition: the choice of the bottom boundary condition is more challeng-
 121 ing, as it requires a model of the karst massif at large scale. For instance, the presence of
 122 underground aquifer would imply a temperature condition. One can also use the estimation
 123 of the underground vertical temperature gradient in typical karst massif. This gradient is
 124 low (about $0.55^\circ\text{C}/100$ m, compared to the usual $3^\circ\text{C}/100$ m geothermal gradient, cf. for
 125 instance [29]). Since this study focuses on the cavity, we neglect the flux at the bottom of the
 126 domain ($z = H$). The influence of this assumption on the estimation of heat transfer in the
 127 shallow cavity is analyzed in the result section. Thus, except when explicitly mentioned, we

128 use

$$\frac{\partial T}{\partial z} \Big|_{z=H} = 0 \quad \text{for } x_{min} < x < x_{max}. \quad (4)$$

129 The last boundary condition for the sub-domain \mathcal{M} concerns the frontier with the cavity \mathcal{C} . The
130 balance of thermal fluxes used to express the coupling between the embedding rock and the cavity
131 is detailed in the next section.

132 2.3. Cavity

133 The cavity is filled with humid air in contact with the cavity wall. Air density decreases when
134 temperature or water vapor concentration increase and several flow regimes may be observed de-
135 pending on the spatial variation of air density in the cave. Air humidity being often close to
136 saturation in closed caves, small temperature differences between wall and air are large enough to
137 induce evaporation or condensation on part of the wall. If the cave floor is colder than the cave
138 ceiling, the configuration is stable and no convection is expected. In the reverse configuration,
139 density gradient in the air may induce convection.

140 In the convective regime, temperature and humidity gradients are mainly localized in thin layers
141 close to the wall, the so-called boundary layers. The characterization of heat and mass transfer
142 through these boundary layers would require to solve Navier Stokes equations, taking into account
143 the variation of air density with temperature and humidity. Corresponding simulations are very
144 time-consuming and thus not compatible with a study over long time scales. Hence we use a
145 simplified description and assume that humid air in the cavity is described by a single temperature
146 $T_a(t)$ and a single water vapor concentration $c_w(t)$. We also assume that (i) air properties do not
147 depend on temperature and humidity, (ii) air is transparent for thermal radiation, (iii) evaporation
148 or condensation takes place at the cavity wall only.

149 The time evolution of T_a results from the convective heat transfer with the cavity wall. With
150 the assumption of a closed cavity, the energy balance reads

$$M_a c_a \frac{dT_a}{dt} = \iint_S \varphi_{conv} dS, \quad (5)$$

151 where M_a is the total mass of air in the cavity, c_a is the air heat capacity at constant pressure
152 ($\text{J.kg}^{-1}.\text{K}^{-1}$), S is the surface of the cavity wall, and φ_{conv} (W.m^{-2}) is the local convective heat

153 flux. It is given by the Newton law,

$$\varphi_{conv} = h_{th}(T - T_a), \quad (6)$$

154 where $T(x, z, t)$ is the local wall temperature. In the simplified model used in this study, the heat
 155 transfer coefficient h_{th} ($\text{W}\cdot\text{m}^{-2}\cdot\text{K}^{-1}$) is assumed constant. The order of magnitude of h_{th} may be
 156 estimated by $h_{th} \sim \lambda_a/\delta_T$, with λ_a ($\text{W}\cdot\text{m}^{-1}\cdot\text{K}^{-1}$) the air conductivity and δ_T the thermal boundary
 157 layer thickness (see Appendix A for more details).

158 The mass balance for water reads

$$V_{cave} \frac{dc_w}{dt} = \rho_w \iint_S v_{ev} dS, \quad (7)$$

159 where V_{cave} is the volume of the cave (i.e. cavity section \times the unit length in the tranverse
 160 direction), c_w is the water vapor concentration ($\text{kg}\cdot\text{m}^{-3}$), ρ_w is the liquid water density ($\text{kg}\cdot\text{m}^{-3}$)
 161 and v_{ev} ($\text{m}\cdot\text{s}^{-1}$) is the local evaporation rate (i.e. the volume of liquid water that evaporates by
 162 unit of time and surface, positive for evaporation).

163 Similarly to the thermal model, we use a description based on a constant mass transfer coefficient
 164 to express the local evaporation rate v_{ev} ,

$$v_{ev} = h_m (c_{sat} - c_w) / \rho_w, \quad (8)$$

165 where h_m ($\text{m}\cdot\text{s}^{-1}$) is the mass transfer coefficient and c_{sat} ($\text{kg}\cdot\text{m}^{-3}$) is the vapor concentration
 166 just above the liquid film on the wall. Evaporation fluxes being very weak, local thermodynamic
 167 equilibrium is assumed at the liquid/gas interface. In the air, the thicknesses of the thermal and
 168 solutal boundary layers are of the same order of magnitude. Thus the mass transfer coefficient may
 169 be estimated by h_m ($\text{m}\cdot\text{s}^{-1}$) $\sim D_w/\delta_T$, where D_w ($\text{m}^2\cdot\text{s}^{-1}$) is the diffusivity of vapor in air [32].

170 Two limiting cases are studied: we consider dry air (i.e. no evaporation or condensation,
 171 $v_{ev} = 0$) or we assume that there is always a liquid film on the wall. We assume that this water film
 172 is thin enough to neglect its conductive thermal resistance compared to the resistance induced by
 173 convection in the air, but thick enough to cover entirely the wall roughness at small scales and to be
 174 considered as a flat film. Thus we do not take into account the Kelvin effect, i.e. the decreasing of
 175 c_{sat} due to the presence of curved interfaces in micro-pores (see [33] for more details). With these

176 assumptions c_{sat} reads

$$c_{sat} = P_{sat}(T) M_w / (R T), \quad (9)$$

177 where R is the gas constant, M_w is the water molar mass and P_{sat} is the saturating vapor pressure
178 at the local temperature of the wall T .

179 The wall boundary condition is provided by the energy balance [34]:

$$\varphi_{cond} = \varphi_{conv} + \varphi_{rad} + \varphi_w \quad (10)$$

180 where φ_{cond} (W.m^{-2}) is the local conductive heat flux coming from the embedding rock, φ_{conv}
181 is the local convective heat flux due to the exchange with the air of the cavity, φ_{rad} is the local
182 net radiative heat flux and φ_w comes from evaporation or condensation latent heat. This equation
183 ensures the coupling between the embedding rock \mathcal{M} and the cave \mathcal{C} .

184 • The conductive flux is

$$\varphi_{cond} = \vec{n} \cdot [-\lambda_r \vec{\nabla} T], \quad (11)$$

185 where \vec{n} is the surface normal vector pointing from the wall towards the cavity, λ_r is the rock
186 conductivity ($\text{W.m}^{-1}.\text{K}^{-1}$) and $\vec{\nabla} T$ is the temperature gradient in the embedding rock at the
187 interface with the gas phase.

188 • The convective flux is given by the Newton law, cf. equation 6.

189 • The net radiative flux is the difference between the emitted and absorbed fluxes. It depends on
190 the wall geometry, radiative properties and temperature. Assuming gray and diffuse surfaces,
191 the following expression is obtained

$$\varphi_{rad} = \epsilon(\sigma T^4 - E), \quad (12)$$

192 where ϵ is the surface emissivity, $\sigma = 5.67 \times 10^{-8} \text{W.m}^{-2}.\text{K}^{-4}$ is the Stefan-Boltzmann con-
193 stant and E is the irradiation (W.m^{-2}) [35]. The determination of E is not trivial, as it
194 must take into account the geometry of the cavity through the view factor evaluation (for
195 instance, some part of a wall may be hidden in case of overhangs). The computation of
196 surface-to-surface radiations is based on the radiosity method.

197 • The last term concerns the heat flux induced by evaporation or condensation on the wall,

$$\varphi_w = L\rho_w v_{ev}, \quad (13)$$

198 where L is the latent heat (J.kg^{-1}).

199 3. Thermophysical properties

200 For the conductivity and diffusivity of the limestone embedding rock, we used $\lambda_r = 1.656 \text{ W.m}^{-1}.\text{K}^{-1}$,
 201 $a_r = 8.10^{-7} \text{ m}^2.\text{s}^{-1}$ (estimated from data of the region of Lascaux in France, cf. Appendix B), in
 202 line with values used in similar karst environments [17, 18]. For air in the cavity, the following data
 203 are used: $\rho_a = 1.23 \text{ kg.m}^{-3}$, $c_a = 1005 \text{ J.kg}^{-1}.\text{K}^{-1}$, $\lambda_a = 0.025 \text{ W.m}^{-1}.\text{K}^{-1}$ (data for $T = 12^\circ\text{C}$
 204 [36, 34]). For water, density ρ_w is 999.5 kg.m^{-3} and latent heat of vaporisation L is $2473.10^3 \text{ J.kg}^{-1}$
 205 (data for $T = 12^\circ\text{C}$ [37, 34]). The diffusivity of vapor in air D_w is $2.43 \cdot 10^{-5} \text{ m}^2.\text{s}^{-1}$ [32]. Tem-
 206 perature variations in the cavity being small, the variation of the saturated vapor pressure with
 207 temperature may be assumed linear. Linearization around the mean temperature ($T_m = 12^\circ\text{C}$)
 208 leads to the following expression (obtained using data from [38]):

$$P_{sat}(T) = a_1 + a_2(T - T_m), \quad (14)$$

209 with $a_1 = 1402.6 \text{ Pa}$, $a_2 = 92.49 \text{ Pa.K}^{-1}$.

210 The emissivity ϵ is close to one for limestone or water for infrared radiation (0.95 and 0.96,
 211 respectively, [39]). As shown in the following, simulations performed for ϵ varying in the interval
 212 $[0.9, 1]$ led to very similar temperature fields. We thus keep $\epsilon = 1$ in the following to model radiative
 213 transfer, except when explicitly mentioned.

214 As detailed in Appendix A, an estimation of the thermal boundary layer thickness, $\delta_T \sim 1 \text{ cm}$,
 215 was obtained from previous simulations of convection performed for Lascaux cave configuration
 216 [3]. Thus the order of magnitude of the heat and mass transfer coefficients are $h_{th} \sim \lambda_a/\delta_T \sim$
 217 $2.5 \text{ W.m}^{-2}.\text{K}^{-1}$ and $h_m \sim D_w/\delta_T \sim 0.0024 \text{ m.s}^{-1}$. In the result section, we refer as the "wet
 218 reference case" the configuration of a cavity filled with humid air, using these values of heat and mass
 219 transfer coefficients and $\epsilon = 1$. The same configuration with $v_{ev} = 0$ is referred as the "dry reference
 220 case". To compare the magnitude of the different heat transfer modes (convection, radiation, phase

change), additional simulations are performed with different values of these parameters.

4. Time constants and humidity in the cavity

Interesting insights can be derived from consideration of model time scales. Equations 5 and 6 with the assumption of constant heat transfer coefficient h_{th} yields

$$\tau_a \frac{dT_a(t)}{dt} = \bar{T}(t) - T_a(t), \quad (15)$$

where $\tau_a = (M_a c_a)/(S h_{th})$ is the thermal time constant of air ($\tau_a \sim 14$ min for the reference case) and

$$\bar{T}(t) = 1/S \iint_S T(x, z, t) dS \quad (16)$$

is the average wall temperature at time t . Using orders of magnitude, one may compare the variation ΔT_a of the air temperature T_a during a given time Δt with the temperature difference $\bar{T} - T_a$. Injecting $dT_a/dt \sim \Delta T_a/\Delta t$ in equation 15 yields

$$\frac{\bar{T} - T_a}{\Delta T_a} \sim \frac{\tau_a}{\Delta t} \sim 10^{-5} \ll 1, \quad (17)$$

where $\Delta t \sim 1$ year has been considered (more rapid fluctuations are damped by heat diffusion in rock). Since the difference between the air temperature T_a and the average wall temperature $\bar{T}(t)$ is much lower than the amplitude of air temperature fluctuations in the cavity, we can do the approximation

$$T_a(t) \simeq \bar{T}(t). \quad (18)$$

Equations 18, 16 and 6 lead to

$$\iint_S \varphi_{conv} dS \simeq 0. \quad (19)$$

The convective heat flux at the cavity wall is thus conservative (the variation of the internal heat stored in the air can be neglected compared with the heat transferred to – or released from – the walls by convection).

The same derivation can be done for the vapor transfer. From equations 7 and 8 and with the assumption of constant mass transfer coefficient h_m , we get

$$\tau_w \frac{dc_w}{dt} = \overline{c_{sat}}(t) - c_w(t), \quad (20)$$

240 where $\overline{c_{sat}}(t) = 1/S \iint_S c_{sat}(x, z, t) dS$ is the average vapor concentration at the wall. The time
 241 constant of the vapor transfer reads $\tau_w = V_{cave}/(S h_m)$ ($\tau_w \sim 12$ min for the wet reference case).
 242 The same analysis as previously done for heat transfer yields

$$c_w(t) \simeq \overline{c_{sat}}(t) \quad \text{and} \quad \iint_S \varphi_w dS \simeq 0. \quad (21)$$

243 The concentration of water vapor in the gas phase can be approximated by the average concentration
 244 at the walls, and the flux of water vapor due to evaporation and condensation is conservative (the
 245 variation of the mass of water stored in the humid air of the cavity is negligible compared with the
 246 water condensed – or evaporated – at the walls).

247 Another consequence of the model assumptions for the wet configuration is that the humidity
 248 Hr remains close to 1. Indeed, the variations of temperature in the cavity being small, c_{sat} in
 249 equation 9 may be approximated by $c_{sat} \simeq P_{sat}(T) M_w/(R \bar{T})$ (because $(T - \bar{T})/\bar{T} \ll 1$). Using
 250 this approximation and equations 14, 18 and 21 we get $c_w \simeq c_{sat}(T_a)$ and

$$H_r = c_w/c_{sat}(T_a) \simeq 1. \quad (22)$$

251 Numerical simulations confirm these results, which are typical of a non-ventilated and humid cavity.

252 5. Numerical method

253 Evaluation of heat and mass transfer in the domain $\mathcal{D} = \mathcal{M} \cup \mathcal{C}$ requires to solve equations 1
 254 to 10.

255 The finite element commercial software Comsol Multiphysics (Galerkin method) was used to
 256 perform numerical simulations. The Comsol "Heat Transfer modulus" takes over the different
 257 modes of heat transfer, including the computation of surface-to-surface radiations, based on the
 258 radiosity method. An irregular mesh was used (with a total of about 11200 Lagrangian quadratic
 259 elements). The mesh was refined close to the top surface and in the vicinity of the cavity.

260 We checked that using a more refined mesh did not change the results. Several tests were also
 261 performed to ensure that: (i) the local energy balance holds (equation 10), (ii) the spatial average
 262 of the net radiative flux is quasi zero at any time (less than $\pm 2 \times 10^{-5} \text{W/m}^2$), (iii) the spatial
 263 average of φ_{conv} and φ_w are both close to zero (less than $\pm 2 \times 10^{-4} \text{W/m}^2$ for the wet reference

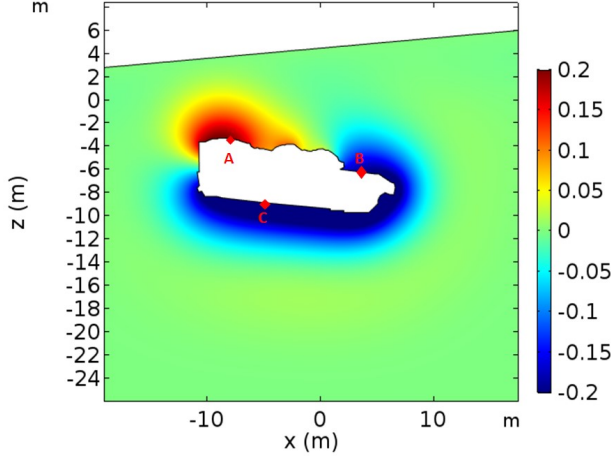


Figure 2: Difference of the temperature fields (color scale on the right in °C) with and without cavity in July. The cavity modifies the karst massif temperature field on a distance of a few meters.

264 case, cf. equations 19 and 21).

265 6. Results for a periodic yearly regime

266 A yearly periodic boundary condition is imposed at the ground surface (cf. equation 3),

$$T_{ex}(t) = T_m + (\Delta T/2) \cos(\omega t), \quad (23)$$

267 where $\omega = 2\pi/\tau$. The period τ is one year. The mean temperature, T_m , is set to 12°C and
 268 $\Delta T = 16^\circ\text{C}$ is the total amplitude of temperature variations.

269 The simulation is started with a uniform temperature equal to T_m in all the computational
 270 domain \mathcal{M} , and a vapor concentration in the cavity corresponding to a humidity of 100% at T_m .
 271 After a transient regime of a few years (not presented in this section), the cavity reaches a periodic
 272 yearly regime. Results presented in the following depict this periodic regime and time evolution
 273 of the variables are drawn for two periods, i.e. 24 months. The highest external temperature
 274 corresponds to $t = 0, \tau, 2\tau$ (cf. equation 23). We assign the highest external temperature to July
 275 and January is therefore the month with the lowest external temperature.

276 *6.1. Spatial distribution and time evolution of the temperature field*

277 First of all, it is interesting to analyze the perturbation induced by the cavity on the temperature
 278 field of the karst massif. An illustration is given in Figure 2 which shows the difference between
 279 the solution with and without cavity for $t = \tau$. In the absence of cavity, heat transfer in the
 280 massif is purely conductive in our model. For the yearly periodic regime, and with the depth of our
 281 computational domain ($H = -40$ m), it can be shown that the solutions corresponding to a semi
 282 infinite medium or to an adiabatic boundary condition at $z = H$ are almost identical [40]. If we
 283 consider a 1D propagative thermal wave from the surface, the analytical solution in the case of a
 284 semi infinite medium is

$$T(d, t) = T_m + \frac{\Delta T}{2} \exp\left(-\sqrt{\frac{\omega}{2a_r}} d\right) \cos\left(\omega t - \sqrt{\frac{\omega}{2a_r}} d\right), \quad (24)$$

285 where d is the distance along the normal to the ground surface ($d = d_v \cos \theta$). The amplitude
 286 of temperature variations decreases strongly with depth, due to the exponential term. Indeed
 287 $\sqrt{\omega/2a_r} = 0.35 \text{ m}^{-1}$ for a period of one year and thus the attenuation factor is $\exp(-0.35 d)$. The
 288 distance d to the ground surface of the three points A , B and C are 7.02 m, 10.87 m and 12.92 m,
 289 respectively. Thus the attenuation factors without cavity are 0.084, 0.022 and 0.01, respectively.
 290 While the oscillation amplitude of the external temperature T_{ex} is $\pm 8^\circ\text{C}$ (cf. equation 23), it drops
 291 to $\pm 0.67^\circ\text{C}$ for point A , and to $\pm 0.08^\circ\text{C}$ for point C . The phase shifts for the three points A , B and
 292 C is 4.7 months, 7.3 months and 8.7 months, respectively (see Figure 3(a)). If the cavity is taken
 293 into account, results are very different as illustrated in Figure 3(b) which shows the time evolution
 294 of the temperature of the three fictive sensors A , B and C with cavity for the wet reference case (as
 295 defined in section 3). The amplitude of oscillation for point A , the closest to the ground surface,
 296 is $\pm 0.36^\circ\text{C}$ when the cavity is present, versus $\pm 0.67^\circ\text{C}$ without cavity. The time corresponding
 297 to the temperature maximum is only slightly modified by the presence of the cavity. The effect
 298 of the cavity is much stronger for points B and C for which temperature are now close to each
 299 other and close to the temperature of point A . Indeed, the maximum of the temperature difference
 300 $T_A - T_C$ drops from $\pm 0.72^\circ\text{C}$ without cavity to $\pm 0.08^\circ\text{C}$ with cavity. As a conclusion, convective
 301 and radiative heat transfers inside the cave homogenize the wall temperature significantly. Another
 302 illustration of the strong homogenisation of temperature induced by the cavity is given in Figure
 303 4. The position on the wall is defined in terms of the curvilinear abscissa $s(x, z)$ (see scheme in
 304 Figure 4). The spatial distributions of the temperature all along the cavity wall are compared for
 305 the configuration with and without cavity, for $t = 4$ months, which corresponds to November.

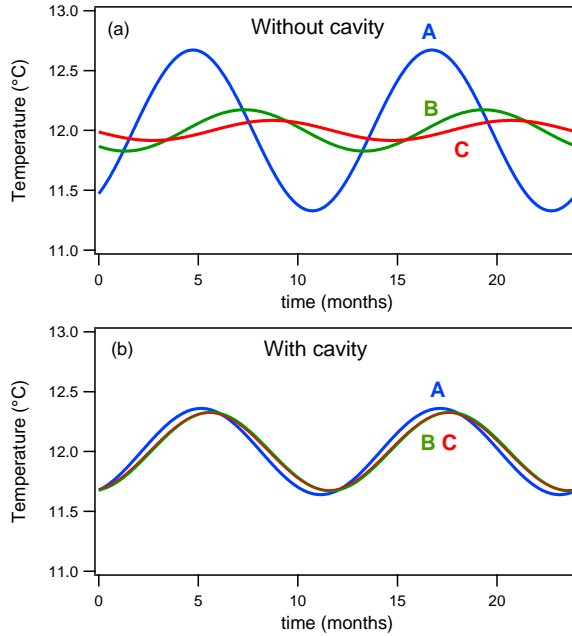


Figure 3: Time evolution (two periods) of the temperature of the three fictive sensors A (blue solid line), B (green solid line) and C (red solid line). (a): case without cavity, (b): cavity for the wet reference case ($t = 0$ corresponds to July, the month with the highest external surface temperature, cf. equation 23). The cave strongly homogenizes the temperature distribution compared to the purely conductive case (without cavity).

306 The spatial distribution of temperature along the cavity wall throughout the year is given in
 307 Figure 5 for the configuration with cavity and for the wet reference case. The external temperature
 308 being a cosine function with a one year period, and the model being quasi-linear, we get $T(s, t) -$
 309 $T_m \simeq -[T(s, t + \tau/2) - T_m]$ with $\tau/2 = 6$ months. Spatial variations are maximal around November
 310 and May, with $T_{max} - T_{min} \simeq 0.17^\circ\text{C}$. July and January show the smallest spatial temperature
 311 variations. Note that due to the phase shift with external temperature, the seasons are quasi
 312 reversed for the cavity compared to the external temperature. July and January are the coldest
 313 and warmest months, respectively.

314 In conclusion, the presence of a cavity significantly affects the spatial repartition of temperature.
 315 The solution corresponding to the pure conductive problem obtained without cavity is thus a poor
 316 approximation of the wall temperature distribution, especially for the temperature of the cave floor.

317 6.2. Relative contributions of the heat transfer modes in the cavity

318 To go further in the characterization of heat and mass transfer, we analyze the relative contri-
 319 butions of the different transfer mechanisms, first for the dry configuration (comparison of radiative
 320 and convective heat transfer) and then introducing evaporation/condensation phenomena.

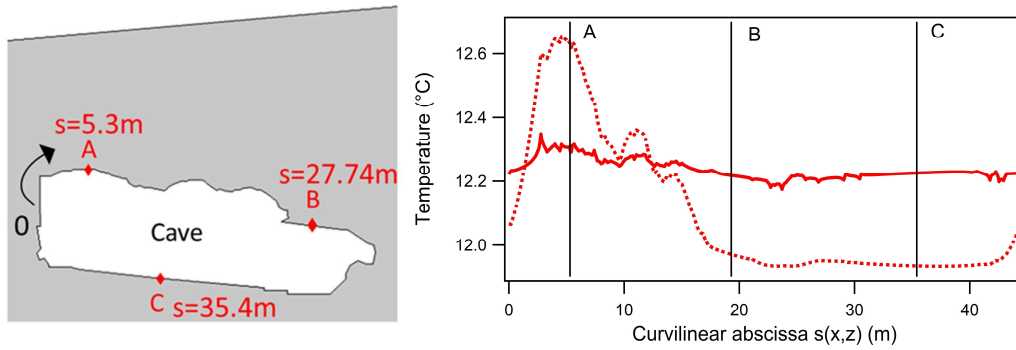


Figure 4: left: Scheme of the curvilinear abscissa $s(x, z)$. The origin of curvilinear abscissa corresponds to the middle height of the left part of the wall and the distance to the origin is covered clockwise - right: spatial distribution of temperature along the wall in November, for the configuration with cavity (wet reference case, red solid line) and without cavity (red dotted line). The position of the three sensors A, B and C is indicated by vertical lines. The spatial variation of temperature is significantly reduced by the presence of the cave.

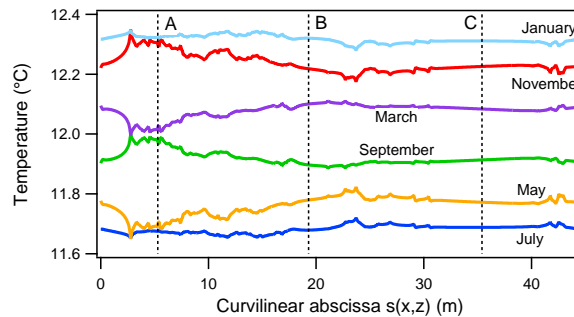


Figure 5: Spatial distribution of temperature along the cavity wall over the year, for the wet reference case. The position of the three sensors A, B and C is indicated by vertical lines. The spatial variations of temperature along the cavity wall vary from month to month, and are maximum in May and November.

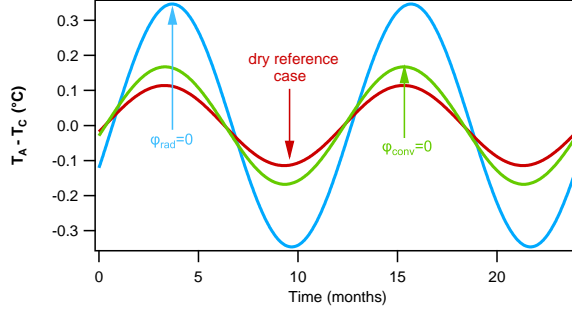


Figure 6: Difference between the wall temperature at points A and C, $T_A - T_C$, for different configurations: dry reference configuration (red solid line, $h_{th} = 2.5 \text{ W.m}^{-2}.\text{K}^{-1}$ and $\epsilon = 1$), non radiative dry configuration (blue solid line, $\varphi_{rad} = 0$) and non convective dry configuration (green solid line, $\varphi_{conv} = 0$). Both radiative and convective heat transfer modes play an important role in the temperature homogenisation, the stronger impact coming from radiative heat transfer.

| case | φ_{rad} | φ_{conv} h_{th} in $\text{W.m}^{-2}.\text{K}^{-1}$ | φ_w h_m in m.s^{-1} | $\max(T_A - T_C)$ $^{\circ}\text{C}$ |
|--------------------|------------------|---|---|---|
| 1. (dry ref. case) | $\epsilon = 1$ | $h_{th} = 2.5$ | 0 | 0.11 |
| 2. | 0 | $h_{th} = 2.5$ | 0 | 0.35 |
| 3. | $\epsilon = 1$ | 0 | 0 | 0.17 |
| 4. | $\epsilon = 1$ | $h_{th} = 0.1$ | 0 | 0.16 |
| 5. | $\epsilon = 1$ | $h_{th} = 1$ | 0 | 0.14 |
| 6. | $\epsilon = 1$ | $h_{th} = 10$ | 0 | 0.06 |
| 7. (wet ref. case) | $\epsilon = 1$ | $h_{th} = 2.5$ | $h_m = 0.0024$ | 0.08 |
| 8. | $\epsilon = 0.9$ | $h_{th} = 2.5$ | 0 | 0.12 |
| 9. | $\epsilon = 0.9$ | $h_{th} = 2.5$ | $h_m = 0.0024$ | 0.08 |

Table 1: Maximal value of the difference $T_A - T_C$ for different cases. The expression of radiative, convective and phase change fluxes are given in equations 12, 6 and 13, respectively.

321 *6.2.1. Dry reference case*

322 In order to assess the relative contribution of convective and radiative transfer, Figure 6 compares
323 the temperature difference between sensors A and C for the following three configurations: (i) dry
324 reference configuration (convective and radiative heat transfer with $h_{th} = 2.5 \text{ W.m}^{-2}.\text{K}^{-1}$ and
325 $\epsilon = 1$), (ii) non radiative dry configuration (convective heat transfer only, $\varphi_{rad} = 0$) and (iii) non
326 convective dry configuration (radiative heat transfer only, $\varphi_{conv} = 0$). These three configurations
327 correspond to cases 1, 2 and 3 in Table 1. Radiative heat transfer, which is always present in a
328 cave, has a stronger impact than the convective heat transfer and leads to temperature difference
329 of $\pm 0.17^\circ\text{C}$ without convection, and to $\pm 0.11^\circ\text{C}$ when both radiative and convective heat transfers
330 are active.

331 As specified in the modeling section, the estimation of convective heat transfer is based on
332 constant coefficients that do not take into account the various regimes of convection occurring
333 throughout the year. Moreover, we only have orders of magnitude for these coefficients. Staying
334 within the framework of this simplified model, we analyze the influence of the convection magnitude
335 by performing new simulations with the following values: $h_{th} = 0, 0.1, 1, 10 \text{ W.m}^{-2}.\text{K}^{-1}$. The
336 highest value, $h_{th} = 10 \text{ W.m}^{-2}.\text{K}^{-1}$, can reasonably be considered as an upper bound for the
337 studied configuration. All these simulations take into account radiative transfer. The maximal
338 value of $T_A - T_C$ as a function of h_{th} is reported in Table 1, cases 1 and 3 to 6. Results for
339 $h_{th} = 0.1 \text{ W.m}^{-2}.\text{K}^{-1}$ and $h_{th} = 0$ are similar and correspond to the case where temperature
340 homogenisation is ensured by radiative heat transfer only. As can be seen, increasing convective
341 heat transfer coefficients result in a decrease of the amplitude of temperature variations which drops
342 from $\pm 0.17^\circ\text{C}$ when only radiative transfer is active to $\pm 0.06^\circ\text{C}$ for $h_{th} = 10 \text{ W.m}^{-2}.\text{K}^{-1}$.

343 The influence of ϵ in the range expected for limestone ($\epsilon > 0.9$) is small, about 0.01°C on the
344 maximal value of $T_A - T_C$ when ϵ decrease from 1 to 0.9 (cf. cases 1 and 8 in Table 1).

345 *6.2.2. Wet reference case*

346 When evaporation and condensation are taken into account, phase change tends to decrease
347 the difference between the wall and air temperatures. Indeed condensation, which occurs when
348 the wall is colder than the air, is exothermic and thus heats the wall. The reverse is expected for
349 evaporation. As a consequence, the spatial variations of temperature are smoothed when phase
350 change occurs. For instance, Table 1 compares the maximal value of $T_A - T_C$ for the dry reference

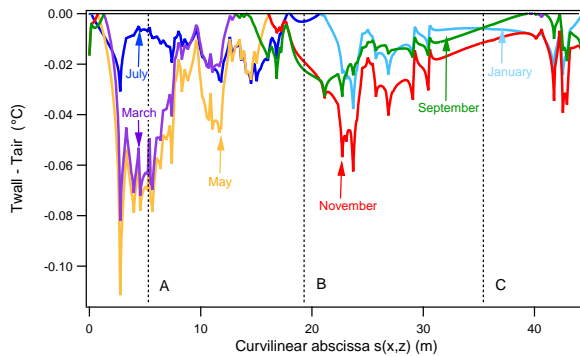


Figure 7: Spatial distribution of the temperature difference between the wall and air in the cavity for the wet reference case. Only negative values are reported on the graph, corresponding to the configuration suitable for condensation on the wall. The position of the three sensors A , B and C are indicated by vertical lines. Magnitude and period of condensation strongly depend on the spatial location.

351 configuration (case 1) and the wet reference configuration (case 7) : $T_A - T_C$ decreases from 0.11°C
 352 to 0.08°C when shifting from the dry to the wet reference cases.

353 In conclusion, radiative transfers cause a significant homogenisation of wall temperature. This
 354 effect is strengthened when convection or phase change are active. In the configuration considered
 355 in this study, the spatial variations of the wall temperature are of the order of 0.1°C .

356 As said in the modeling section, the wet reference case corresponds to a case without limitation
 357 of water supply, i.e. there is a permanent water film on the wall. Thus this configuration max-
 358 imises the condensation or evaporation time durations. Though small, the temperature differences
 359 between wall and air are high enough to cause significant fluxes of evaporation ($T_{wall} - T_a > 0$) or
 360 condensation ($T_{wall} - T_a < 0$). The temperature difference between wall and air for the configura-
 361 tion suitable to condensation is given in Figure 7. Condensation is observed mainly in March and
 362 May at the upper part of the cave roof (point A), while it is observed in November in the lower
 363 part of the cave roof (near point B at $s \sim 23\text{m}$). The temperature difference is smaller at the
 364 cave floor (point C). The evaporation rate throughout the year is shown in Figure 8 for the three
 365 probes. The model shows that periods of several consecutive months of significant condensation
 366 (or evaporation) may be observed on the same part of the wall (cf. for instance sensor A in Figure
 367 8, for which the condensation rate is greater than $2\mu\text{m}/\text{day}$ for about five months). Depending on
 368 the location in the cave, this may produce a few tenth of millimeter of water on the cave walls.
 369 This result is important as some phenomena occurring on the wall (carbonate dissolution [41], clay
 370 swelling ...) may be strongly sensitive to the flow rate of condensation water. In order to get
 371 an upper bound of condensation fluxes, an additional simulation was performed using an estima-

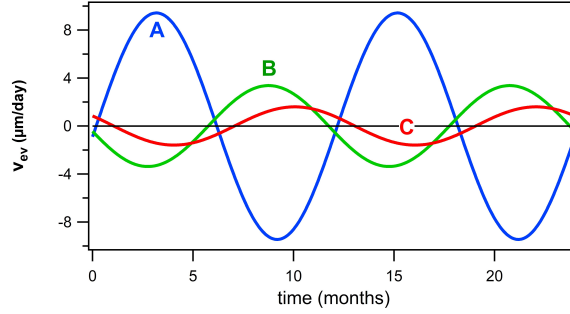


Figure 8: Time evolution of the evaporation rate v_{ev} (in $\mu\text{m}/\text{day}$) for the wet reference configuration, for sensor A (blue solid line), B (green solid line) and C (red solid line). By convention, v_{ev} is positive for evaporation and negative for condensation. Succession of condensation and evaporation periods of several months are observed.

372 tion of the upper bounds of these coefficients, that is four times the values of the wet reference
 373 case: $h_{th} = 10 \text{ W}\cdot\text{m}^{-2}\cdot\text{K}^{-1}$ and $h_m = 0.0096 \text{ m}\cdot\text{s}^{-1}$. The evaporation rate is thus higher, close to
 374 $\pm 14 \mu\text{m}/\text{day}$ for sensor A .

375 The orders of magnitude of condensation rates are similar to experimental estimations performed
 376 in other caves: in the Kartchern cave in Arizona, Buecher [42] reports a condensation rate which
 377 varies from 0 to about $15 \mu\text{m}/\text{day}$ during the year. Measurements performed in the Glowworm cave
 378 in New Zealand by De Freitas and Schmekal [22] in the Banquet Chamber gives values from 0 to
 379 about $12 \mu\text{m}/\text{day}$, when the Chamber was isolated from outside by a door.

380 The time evolution of the four different fluxes involved at the cave wall (conductive, convective,
 381 radiative and phase change) are given in Figure 9 for the wet reference case and for the three
 382 sensors. Due to the underlying assumptions (periodic boundary condition at the ground surface,
 383 zero flux at the bottom of the karst massif, quasi linear model), the fluxes at a given point are
 384 also periodic with a zero mean value. Depending on the location on the wall, they can be inphase
 385 (for instance sensors A and C) or shifted (sensor B). Their magnitude depends also on the sensor
 386 location. The highest fluxes are observed as expected at sensor A which is closer to the ground
 387 surface. Very few evaporation/condensation phenomena ($\varphi_w \simeq 0$ throughout the year) are observed
 388 on the cave floor (sensor C). It is interesting to note that succession of wet and dry periods is a
 389 known phenomenon that may be observed on some cave walls, including Lascaux cave. It would be
 390 interesting to compare simulations to observed time and spatial evolution of wall humidity. However
 391 such a comparison would require to shift to a more realistic 3D geometry.

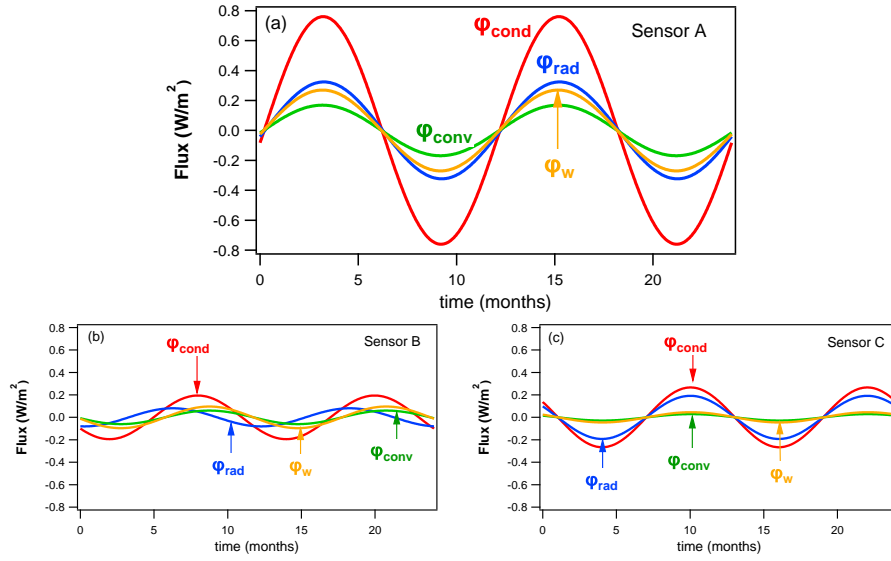


Figure 9: Time evolution of the different fluxes for the wet reference case, for sensors A (a), B (b), C (c). At any time, the conductive flux (red solid line) is the sum of the convective flux (green solid line), radiative flux (blue solid line) and evaporation/condensation flux (orange solid line). The highest fluxes are observed at sensor A which is closer to the ground surface than sensors B and C.

392 *6.2.3. Influence of the geothermal flux*

393 As observed in Figure 9 the fluxes are weak, less than 1 Wm^{-2} . However, the maximal values of
 394 the conductive flux at the wall are much greater than the geothermal flux that has been neglected
 395 in our model. Indeed the conductive flux corresponding to a gradient of $3^\circ\text{C}/100 \text{ m}$ would be about
 396 0.05 Wm^{-2} . A simulation was performed by imposing a constant flux of 0.05 Wm^{-2} at the bottom
 397 of the computational domain ($z = H$). The mean yearly temperature in the massif is therefore no
 398 more equal to the mean external temperature ($T_m = 12^\circ\text{C}$) and increases with depth. Without
 399 cavity, it increases from 12.21°C for sensor A to 12.39°C for sensor C. With the cavity and for
 400 the wet reference case, homogenisation induced by the cavity results in a mean yearly temperature
 401 of 12.31°C for sensor A and 12.32°C for sensor C. The geothermal flux does not change much
 402 the magnitude of the cavity wall temperature spatial repartition, compared to the adiabatic case
 403 considered in the previous sections. Indeed, $T_A - T_C$ varies from -0.09°C to 0.07°C during one
 404 year, while it is between $\pm 0.08^\circ\text{C}$ for the adiabatic case. This validates the approximation of zero
 405 flux used as boundary condition at the bottom of the karst massif in most of the simulations of the
 406 periodic yearly regime, as soon as the present study concerns the analysis of the main trends of
 407 heat and mass transfer in a shallow cavity.

408 7. Simulations with real climatological data

409 7.1. Available data

410 Simulations of the thermal response of the cave are performed using real meteorologic data
411 for the temperature boundary condition imposed at the surface of the massif (equation 3). To
412 get a long period of available measurements, we used the data of Gourdon’s weather station
413 ($44^{\circ}44'42''\text{N}$, $1^{\circ}23'48''\text{E}$), located at a distance of about 150 km from Lascaux ($45^{\circ}3'14''\text{N}$, $1^{\circ}10'3''\text{E}$).
414 The altitudes are 260 m and 185 m for Gourdon and Lascaux, respectively. The data of the two
415 locations are correlated [43], but the temperature recorded at Lascaux is often lower. The monthly
416 average external temperatures in Gourdon for the period 1941-2017 were provided courtesy of
417 ”Météo-France” and are displayed on Figure 10 (a). These monthly data were used to compute the
418 yearly average temperature (Figure 10 (b)). The lowest yearly average temperature is observed in
419 1956 (10.9°C) and the highest in 2011 (14°C). A slight warming trend may be observed during
420 about the last thirty years. The fluctuation amplitude over one year, corresponding to the difference
421 between the hottest and coldest months for each year, is given in Figure 10 (c). It varies a lot from
422 one year to another, for instance 12.6°C in 2002 and 22.7°C in 2012.

423 7.2. Influence of the initial state and boundary condition

424 Unlike for the yearly periodic regime, the choice of the initial temperature field and of the bound-
425 ary condition at the bottom of the computational domain is challenging for simulations with real
426 data containing temperature variations over long time scales (e.g. decadal temperature variations).
427 Indeed, for the yearly periodic regime studied in section 6, the depth of the computational domain
428 ($H = -40\text{ m}$) was large enough to be insensitive to yearly fluctuations. The mean temperature
429 $T_m = 12^{\circ}\text{C}$ was chosen as initial condition for the whole domain. As this value remained the same
430 from one year to the next, the effect of the initial condition was sensitive over a few years only and
431 the periodic regime was rapidly achieved.

432 This is no longer the case with real data as the yearly average temperature shows potentially
433 long-term temporal variations. Therefore, fluctuations of the temperature field can penetrate deeper
434 in the karstic massif. In addition the temperature field inside the massif at the beginning of the data
435 set (1941) is unknown and results from the prior thermal history. Thus a sensitivity analysis was
436 performed in order to evaluate the impact of the initial condition and bottom boundary condition
437 on simulations with real meteorologic data. Three scenarios have been tested: (i) The first scenario

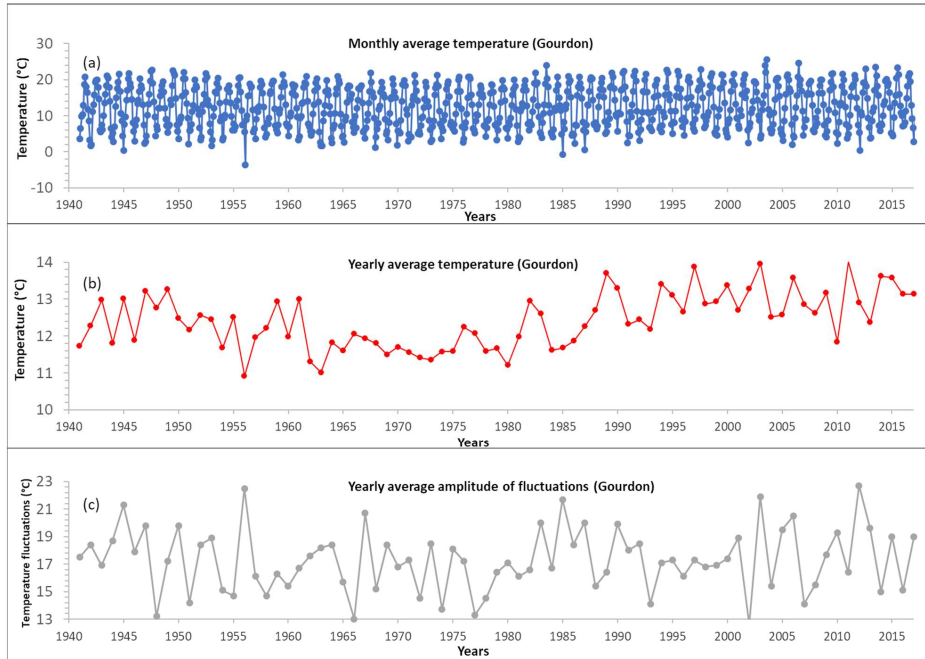


Figure 10: Gourdon's weather station. (a): monthly average external temperature. (b): yearly average external temperature (c) yearly amplitude of fluctuations estimated from monthly average temperature (difference between the hottest and coldest months for each year).

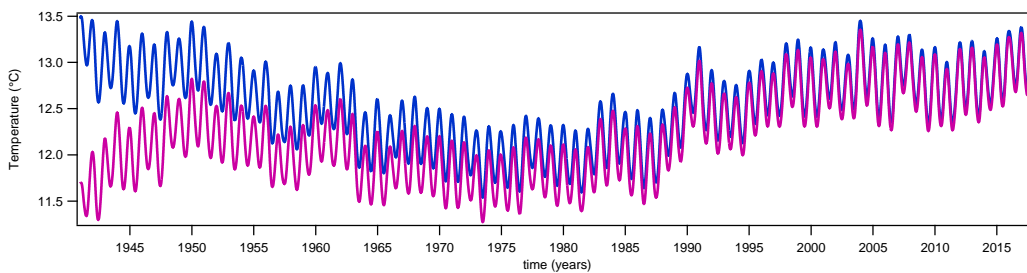


Figure 11: Simulations of the time evolution of the temperature at point A for the wet reference case and scenario (i) with two initial conditions: $T = 11.7^{\circ}\text{C}$ (magenta continuous line) and $T = 13.5^{\circ}\text{C}$ (blue continuous line). Due to the large time constant of the diffusive mass, a few decades are needed to make the signal independent on the initial condition.

438 corresponds to the configuration used in most of the previous simulations, with a zero flux boundary
 439 condition at $z = H = -40$ m. The initial condition is assumed uniform in the massif, and two values
 440 have been tested. One is 11.7°C , which is the average temperature for the year 1941, corresponding
 441 to one of the lowest observed on the available times series. Another one is 13.5°C , which belongs
 442 to the highest observed values. (ii) In the second scenario the zero flux boundary condition is
 443 imposed at greater depth, at $z = -100$ m. (iii) In the third scenario, a constant flux of 0.05Wm^{-2}
 444 (geothermal flux) is imposed at $z = H = -40$ m. For this third scenario, the initial temperature is
 445 set to 11.7°C or 13.5°C at the ground surface, and increases linearly with depth. For all the tests,
 446 the 77 years of Gourdon’s data have been used as boundary condition at the ground surface, and
 447 the parameters are those of the wet reference case.

448 For the first scenario, Figure 11 shows the time evolution of the temperature at point A for
 449 the two different initial conditions. As can be seen, the initial condition affects the results over a
 450 long period. About fifty years of simulation are needed for the gap between the two simulations
 451 to become lower than 0.25°C . The slow increase of the average temperature observed during the
 452 period 1988-2017 is correlated with the behavior of the external temperature.

453 The influence of the initial condition needs more time to disappear in the second scenario as a
 454 larger depth is involved, and the difference on T_A with the two initial conditions is still 0.38°C in
 455 1990 (results not shown here). Figure 12 gathers the results of the six tests (3 scenarios and two
 456 initial conditions) for the temperature at point A for the last fourteen years. As can be seen, the
 457 general time evolution is the same for all the tests. For instance, the existence of a warmer year in
 458 the cavity in 2007 is obtained for all the simulations. But the discrepancy on the temperature value
 459 between the six tests is rather large, about 0.4°C between the two extreme configurations. This
 460 value is of the same order as the amplitude of temperature variations between winter and summer,
 461 from 0.5°C to 0.9°C depending on the year.

462 However, the uncertainty on the initial temperature and the boundary condition affects only
 463 slightly the temperature difference along the cavity wall. Figure 13 shows the difference $T_A - T_C$
 464 for the six tests along the last fourteen years. The amplitude of variation of $T_A - T_C$ varies from
 465 about 0.12°C to 0.16°C (depending on the year) for all the tests. These values are close to the one
 466 obtained in the yearly periodic case. Indeed, even if the annual temperature fluctuations at Gourdon
 467 change from one year to another (Figure 10 (c)), their average value is close to the amplitude of
 468 the external temperature in the yearly periodic regime (16°C , cf. equation (23)).

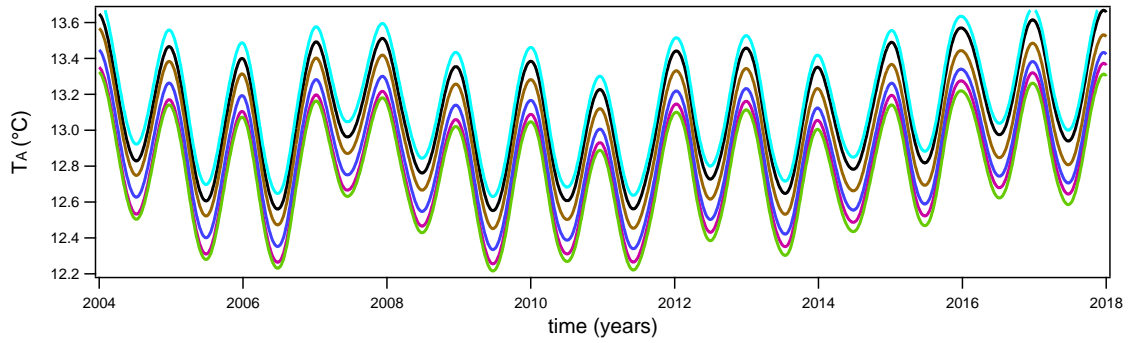


Figure 12: Simulations of the temperature T_A for the three scenarios and two different initial conditions. From top to bottom: scenario (iii) with $T = 13.5^\circ\text{C}$ (light blue continuous line), scenario (iii) with $T = 11.7^\circ\text{C}$ (black continuous line), scenario (ii) with $T = 13.5^\circ\text{C}$ (brown continuous line), scenario (i) with $T = 13.5^\circ\text{C}$ (blue continuous line), scenario (i) with $T = 11.7^\circ\text{C}$ (magenta continuous line), scenario (ii) with $T = 11.7^\circ\text{C}$ (green continuous line). The general trend is the same for all the tests, but significant differences on the temperature are observed between the different tests.

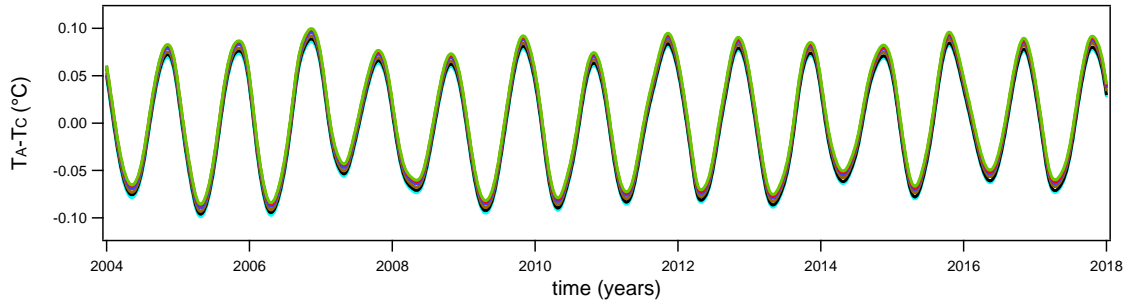


Figure 13: Simulations of the temperature difference $T_A - T_C$ for the three scenarios and two different initial conditions: scenario (iii) with $T = 13.5^\circ\text{C}$ (light blue continuous line), scenario (iii) with $T = 11.7^\circ\text{C}$ (black continuous line), scenario (ii) with $T = 13.5^\circ\text{C}$ (brown continuous line), scenario (i) with $T = 13.5^\circ\text{C}$ (blue continuous line), scenario (i) with $T = 11.7^\circ\text{C}$ (magenta continuous line), scenario (ii) with $T = 11.7^\circ\text{C}$ (green continuous line). The six curves are very close, which means that the difference $T_A - T_C$ is little sensitive to the initial conditions in the massif.

469 As a conclusion, due to the uncertainty on the thermal history of the massif, the model does not
 470 provide an accurate estimate of the wall temperature at a given point. However, it gives information
 471 on global climatological trends in the cavity and on the spatial variations of wall temperature, which
 472 is an important point to estimate evaporation/condensation rate. Finally, for future studies, these
 473 results underline the importance of deepening the knowledge of heat transfer in karst massif to
 474 improve the choice of a pertinent boundary condition.

475 7.3. Comparison with Lascaux cave data

476 The geometry used in our simulations (2D closed cavity) is a simplified scheme of the real
 477 passage in Lascaux cave ("the Hall of Bulls"). Several other simplifying assumptions have also
 478 been made, so that the results analysed in the previous sections may be viewed as extreme cases of

479 the real configuration. Indeed, the cavity is assumed to be closed, despite the fact that exchanges
480 with lateral passages exist seasonally, as evidenced by the analysis of the space and time evolution
481 of the CO₂ pressure recorded in several locations in the cavity [43, 41]. Small exchanges with
482 the outdoor air may also occur. Using external temperature data as boundary condition for the
483 ground temperature is also an approximation, and a more realistic simulation would require to
484 take into account sunshine, inhomogeneity in the ground vegetation cover etc (cf. for instance
485 [44, 45, 46]). However, as we only focus on the main characteristics of the climate in the cavity,
486 it is anyways interesting to compare simulations with field data, to see to what extent the general
487 trends obtained with our model are observed in the real cavity and to what extent the simplified
488 conditions considered in the simulations reflect the thermal behavior of the cavity.

489 We use experimental data of two sensors located on the ceiling and floor of the Hall of Bulls,
490 approximately in the middle of the Hall.

491 Temperature simulations at point *A* and *C* (scenario (i) with $T = 11.7^\circ\text{C}$ as initial condition)
492 and measured temperature at the ceiling and floor sensors are displayed in Figure 14. Simulated
493 temperatures follow very well the general trend of the experimental data. For instance the warmer
494 years 2007 and 2008 are observed both in simulated and experimental temperatures, and the increase
495 of the average temperature observed during the last four years is also obtained in the simulations.
496 This means that the diffusive equation used to model heat transfer in the embedding rock is suitable
497 for Lascaux cave. Experimental temperatures are lower than the simulated ones, which may be
498 partly due to the uncertainty on the initial state (cf. section 7.2) and partly to the differences
499 between Gourdon and Lascaux external temperatures in recent years. Indeed average yearly external
500 temperatures recorded at Lascaux from 2012 to 2017 are for instance about 0.7°C lower than those
501 of Gourdon.

502 As can be seen, simulations overestimate the seasonal temperature fluctuations, which are about
503 0.6°C between summer and winter for point *A*, while they are of the order of 0.4°C for the ceiling
504 measured temperatures. Simulations also underestimate the temperature difference between the
505 roof and ceiling: the temperatures of the two points *A* and *C* (magenta and gray lines) are very
506 close to each other, compared to the measurements at the ceiling and floor (green and brown dots).

507 This is due to the simplified assumptions (geometry and air description) used in the model.
508 First, one may expect that radiative heat transfers are slightly overestimated in the 2D model used
509 in the simulations. The real cavity is indeed 3D, with a more tortuous geometry than the one

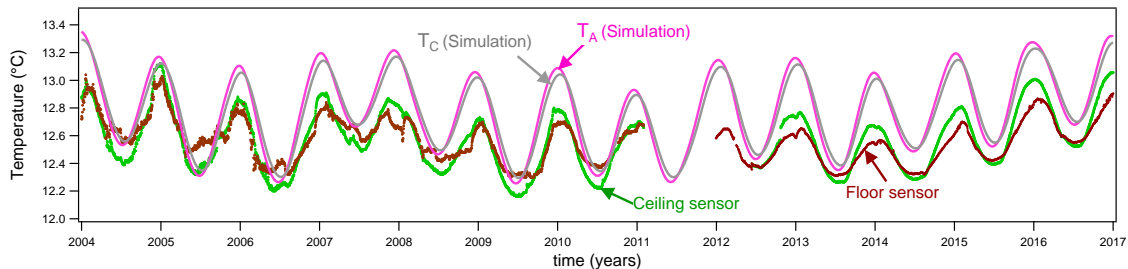


Figure 14: Comparison between simulations (scenario (i), $T = 11.7^\circ\text{C}$) and Lascaux cave measurements: simulated T_A (magenta solid line), simulated T_C (gray solid line), Lascaux ceiling measurements (green dots), Lascaux floor measurements (brown dots). The main trends are well reproduced by the model, however we observe lower seasonal variations and higher temperature difference between the floor and ceiling in the real cavity, compared to the 2D simulations.

510 used in the simulations. The presence of side walls connecting the floor to the ceiling, and the
 511 complex geometry (some parts of the wall are not facing each other) will modify the magnitude and
 512 repartition of radiative heat transfer and will reduce the homogenisation of the temperature wall.
 513 A planned extension of the present model is thus to shift to a 3D geometry, close to the real cavity
 514 configuration.

515 A second point concerns the assumption of a unique air temperature, which means that air
 516 is thoroughly mixed, and the assumption of constant heat transfer coefficient. The challenge is
 517 to improve the description of convection, while maintaining a model light enough to allow long
 518 term simulations. For this purpose, preliminary simulations of air convection using Navier Stokes
 519 equations and coupling the cavity with the massif are planned, in order to characterize the seasonal
 520 evolution of natural convection in the cavity. The objective is to build a reduced model from the
 521 detailed simulations, closer to real configurations than the current model. For instance it may
 522 include heat and mass transfer coefficients that change according to each season or according to
 523 the location on the wall.

524 8. Conclusion and outlook

525 We have developed a coupled model of heat and mass transfer in a shallow and non-ventilated
 526 cave embedded in a karst massif. The model takes into account conductive transfer in the karst
 527 massif, convective and radiative transfer in the cavity and evaporation/condensation at the cavity
 528 wall. First simulations have been performed for a periodic Dirichlet condition at the ground surface
 529 and we analyzed the corresponding periodic regime in the cavity. Results demonstrate that the
 530 temperature field is significantly deformed compared to the case without cavity. Fluxes at cave

531 wall, related to radiation, air-convection and evaporation/condensation (in case of a humid cave)
532 all contribute to a significant homogenization of wall temperatures, with an important contribution
533 of radiative transfer, which can never be neglected. In case of high humidity, simulations of evap-
534 oration/condensation periods show that some parts of the wall may be durably (several months)
535 subjected to significant condensation (or evaporation).

536 Real meteorological data, 77 years of external temperature data of the Gourdon station in
537 France, have been used as input of the model. Results of simulations have been compared to exper-
538 imental temperature of Lascaux cave, with good agreement considering the simplifying hypotheses
539 assumed for this modeling. The asset of such a model is the low computing time required to sim-
540 ulate several years, and thus its ability to follow long time evolution. Further investigations are
541 planned to improve the description of the temperature field while maintaining reasonable computing
542 times, taking into account 3D geometry, seasonal changes in the convective regime and the ground
543 vegetation cover.

544 The alternation of condensation and evaporation is a factor of wall weathering by calcite dis-
545 solution and precipitation. Humidity is furthermore a factor controlling ecosystems, leading to a
546 specific microbiology associated to this environment, which in turns represents a further potential
547 weathering agent. Concerning evaporation/condensation two configurations have been considered
548 in the model, the dry reference case (no water in the cavity) and the wet reference case (without
549 water limitation, i.e. there is always a water film on the wall). In this last configuration, the
550 modeling shows that duration and intensity of condensation/evaporation events highly depend on
551 the position of the spot considered on a cave wall. Two nearby areas on the wall may differ from
552 a climatological and ecosystemic point of view. The present paper shows that the modeling of
553 this pattern is complex, nevertheless possible. Indeed, in a real configuration, the cavity should be
554 situated between the dry (no water) and wet (no limitation on water) reference cases. This may
555 be taken into account in the model, provided that data on the availability of water throughout the
556 year are known. This may be a complex problem, which requires the estimation (or the model-
557 ing) of the exchanges with the embedding rock (water percolating through the massif) or direct
558 water exchanges with external air for which humidity changes during the year (cf. for instance the
559 study of Li and co-authors [45, 46] where the heat and moisture transfer in the surrounding soil are
560 considered).

561 Results significantly improve our understanding of conditions taking place in a shallow cavity,

562 what will help improving the management of caves, especially those with very fragile decorations
563 such as Paleolithic paintings. It may also be useful for managing shallow underground constructions
564 (e.g. a mine or even a cellar). For Lascaux cave, it will guide us to identify areas which are the most
565 exposed to weathering and to test the effect of past and potential changes in nearby conditions.
566 The modeling was focused on the case of a shallow and confined cave. In this situation heat is fully
567 transferred from the surface to the cave through the rock-matrix. Results cannot be transferred
568 directly to the case of a ventilated cave where heat is more significantly transferred by air circulation.
569 Condensation and evaporation fluxes are expected to be even more important than in a confined
570 cave, providing a clear motivation for expanding the modeling to other conditions.

571 **Acknowledgments**

572 The study is part of investigations supported by the French Ministry of Culture, Direction des
573 Affaires Culturelles de Nouvelle-Aquitaine. We want to thank them and their sub-contractants
574 for support and data. In this context we want to thank more specifically Jean-Christophe Portais
575 and Sandrine Géraud for their help. We also thank Météo France which provided Gourdon's
576 meteorological data within the framework of French research support.

577 **Appendix A. Estimation of the convective heat transfer coefficient**

578 The convective heat transfer coefficient is difficult to evaluate because it is a local quantity which
579 depends on many parameters, including the global geometry of the system and the local surface
580 morphology of the walls. The geometry of real caves is extremely complex, but as part of the
581 simplified model developed in this paper, we can provide an order of magnitude of this coefficient.

582 A scale analysis of the heat flux transferred from a wall to the adjacent fluid [36] shows that the
583 order of magnitude of the convective heat transfer coefficient, h_{th} , is

$$h_{th} \sim \frac{\lambda_a}{\delta_T} \tag{A.1}$$

584 where λ_a is the thermal conductivity of air ($\lambda_a = 0.025 \text{ W.m}^{-1}.\text{K}^{-1}$) and δ_T is the thermal boundary
585 layer thickness, i.e. the region in which the temperature changes from T_w at the wall to T_a far from
586 the wall. In a convective heat transfer problem, the challenge is then to determine δ_T scaling, which
587 depends on the characteristic parameters of the system. For air, the Prandtl number (i.e. the ratio
588 between momentum and thermal diffusivities) is of order unity which means that δ_T is of the same

589 order as the velocity boundary layer thickness δ .

590 Air motion in a cave is mainly driven by the buoyancy effect due to the presence of density
 591 variations between the different areas of the cave. A convection flow can develop on a large scale
 592 (cave scale) which can be locally seen as a forced convection flow, for example in narrow passages,
 593 or as a natural convection flow along the vertical walls in larger areas.

594 If the air flow is considered as a forced convection flow, the velocity boundary layer thickness δ ,
 595 i.e. the region in which the velocity changes from zero at the wall to u_∞ far from the wall, depends
 596 on the Reynolds number, $\mathcal{R}e_L = u_\infty L / \nu_a$ with ν_a the kinematic viscosity of air ($\nu_a \sim 10^{-5} \text{ m}^2 \cdot \text{s}^{-1}$)
 597 and L the characteristic length of the system. Numerical simulations performed by Malaurent et
 598 al. [4] in the Lascaux cave show that the order of magnitude of the velocity in narrow passages
 599 is 10 cm/s. By choosing $L \sim 1$ m, the characteristic length over which the wall of a cave can be
 600 considered as flat, we obtain $\mathcal{R}e_L \sim 10^4$. The flow is therefore laminar ($\mathcal{R}e_L \lesssim 10^5$). Based on a
 601 scale analysis of the terms involved in the momentum conservation equation of a forced flow along
 602 a flat plate [36], we can estimate the order of magnitude of the laminar boundary layer thickness:

$$\delta \sim L \mathcal{R}e_L^{-1/2} \tag{A.2}$$

603 For $\mathcal{R}e_L \sim 10^4$ and $L \sim 1$ m, we obtain $\delta \sim 1$ cm hence $\delta_T \sim \delta \sim 1$ cm.

604 If we now consider a natural convection flow, the air motion is generated by the difference in
 605 density, $\Delta\rho$, between the air in contact with the wall and the air away from the wall. Let us assume
 606 that this difference is induced by temperature variations only (thermal convection). The thermal
 607 boundary layer thickness δ_T depends on the thermal Rayleigh number $\mathcal{R}a_L = g(\Delta\rho/\rho)L^3/(D_{th}\nu)$,
 608 with g the gravitational acceleration and D_{th} the thermal diffusivity.

609 Considering $T_w - T_a \simeq 0,1$ °C, we estimate $\Delta\rho/\rho \sim 10^{-4}$. For a characteristic length scale
 610 $L \sim 1$ m, $\nu \sim D_{th} \sim 10^{-5} \text{ m}^2 \cdot \text{s}^{-1}$, $g \simeq 10 \text{ m} \cdot \text{s}^{-2}$, we obtain $\mathcal{R}a_L \sim 10^7$. The flow is therefore
 611 laminar ($\mathcal{R}a_L \lesssim 10^9$). Based on a scale analysis of the terms involved in the coupled momentum
 612 and energy conservation equations of a natural convection flow along a vertical flat plate of height
 613 L [36], we estimate the order of magnitude of the laminar boundary layer thickness for air:

$$\delta_T \sim L \mathcal{R}a_L^{-1/4} \tag{A.3}$$

614 For $\mathcal{Ra}_L \sim 10^7$ and $L \sim 1$ m, we obtain $\delta_T \sim 1$ cm.

615 It is also possible to estimate the order of magnitude of the velocity in the boundary layer:
616 $v \sim \sqrt{g(\Delta\rho/\rho)L} \sim 3$ cm/s. This value corresponds to the magnitude of the velocity calculated near
617 the vertical walls of the "Hall of Bulls" reported by Malaurent et al. [4, 3]. Using helium filled
618 balloons, Schoeller [30] made some estimations of the air velocity at the ceiling, and obtained values
619 from about 6 cm/s to about 20 cm/s.

620 As a conclusion, for the two possible convection regimes the order of magnitude of the thermal
621 boundary layer thickness is $\delta_T \sim 1$ cm, which yields to an estimation of the convective heat transfer
622 coefficient using equation A.1 : $h_{th} \sim 2.5$ W.m⁻².K⁻¹.

623 It is important to be aware that the value given above for h_{th} is not a precise value but only an
624 order of magnitude which reflects a very simplified description of the convection heat fluxes that
625 occur in caves.

626 **Appendix B. Estimation of the limestone rock diffusivity**

627 The estimation of the rock diffusivity a_r is based on temperature measurements performed
628 during about 22 months in the karst massif, a few tens of meters away from the Lascaux cave
629 (provided courtesy of the technical staff of Lascaux cave). The sensors used for this purpose
630 are located vertically inside the massif, at depths $z_1 = -1.5$ m, $z_2 = -2.3$ m, $z_3 = -3.2$ m and
631 $z_4 = -4$ m.

632 Assuming 1D conduction heat transfer between the four sensors, the temperature field in the
633 domain $z_1 \geq z \geq z_4$ is described by the conduction equation

$$\frac{\partial T}{\partial t} = a_r \left(\frac{\partial^2 T}{\partial z^2} \right). \quad (\text{B.1})$$

634 The temperatures of the two sensors located at $z_1 = -1.5$ m and $z_4 = -4$ m are used as Dirichlet
635 boundary conditions at the frontier of the domain, for $0 \leq t \leq \Gamma$, with $\Gamma = 667$ days. The initial
636 condition, $T(z, t = 0)$, is fitted by interpolation between the four sensors. With these initial and
637 boundary conditions, the temperature field for $z_1 > z > z_4$ is obtained by solving equation B.1.
638 The temperatures resulting from the simulation for the two sensor positions $z_2 = -2.3$ m and
639 $z_3 = -3.2$ m and for $0 \leq t \leq \Gamma$, are noted $T_{sim2}(t)$ and $T_{sim3}(t)$.

640 Simulations are performed for different values of the diffusivity a_r . The value of a_r that will be
641 adopted for the limestone massif is the one which minimizes the difference between the simulated
642 values, $T_{sim2}(t)$ and $T_{sim3}(t)$, and the experimental data at the same depths, $T_{mes2}(t)$ and $T_{mes3}(t)$.
643 To this end, the errors $ER2$ and $ER3$ are estimated by the following expressions

$$ER2(a_r) = \left[\frac{1}{\Gamma} \int_0^\Gamma (T_{sim2}(t) - T_{mes2}(t))^2 dt \right]^{1/2}, \quad (\text{B.2})$$

644 which is approximated by

$$ER2(a_r) \simeq \left[\frac{1}{N} \sum_{i=1, N} (\tilde{T}_{sim2}(t_i) - \tilde{T}_{mes2}(t_i))^2 \right]^{1/2} \quad (\text{B.3})$$

645 with $t_i = i\delta t$ where δt is the sampling time and \tilde{T} the average temperature over δt . At depths
646 $z < z_1 = -1.5$ m, high frequency fluctuations of external temperature are filtered and we choose
647 $\delta t = 24$ h. $\Gamma = N\delta t$, with $N = 667$.

648 The same procedure is performed for $ER3$. The figure B.15 gives the sum $ER2 + ER3$ as a
649 function of the diffusivity a_r . The minimal value of the error is about 0.35°C and is obtained
650 for $a_r \simeq 8 \times 10^{-7} \text{m}^2.\text{s}^{-1}$. It corresponds to $ER2 \simeq 0.15^\circ\text{C}$ and $ER3 \simeq 0.2^\circ\text{C}$. For this value of
651 the diffusivity, Figure B.16 shows the simulated and measured temperatures for the two sensors.
652 Given the uncertainty on the exact position of the sensors, the comparison between simulated and
653 measured temperatures can be considered satisfactory and $a_r = 8 \times 10^{-7} \text{m}^2.\text{s}^{-1}$ is used in the
654 simulations.

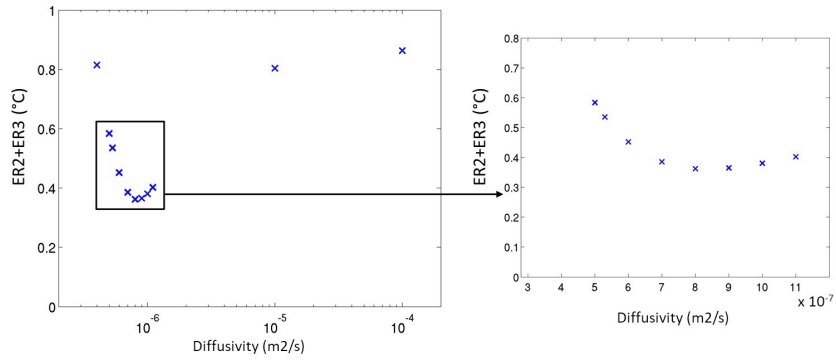


Figure B.15: Difference between simulated and measured temperatures, ($ER2 + ER3$), as a function of the limestone diffusivity. Left: semi-log scale - Right: zoom on the outlined rectangle, with linear scale.

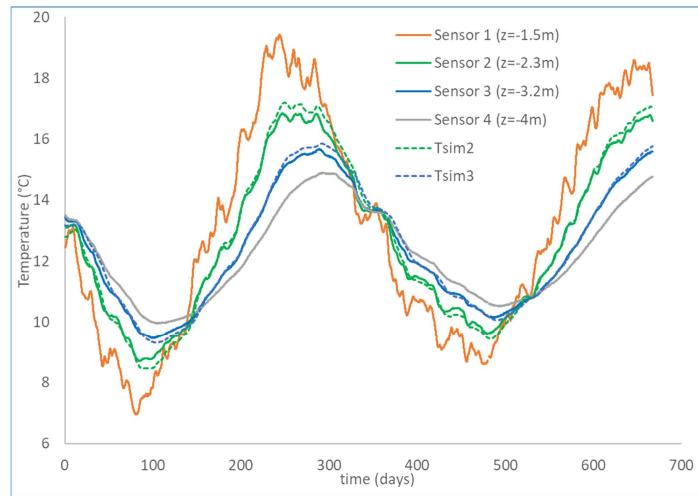


Figure B.16: Comparison between experimental data (continuous lines) and simulated temperatures (dotted lines) for sensors 2 and 3, with $a_r = 8 \times 10^{-7} \text{m}^2 \cdot \text{s}^{-1}$. The data corresponding to sensors 1 and 4 are used as boundary conditions of the 1D conductive model.

655 **References**

- 656 [1] L. Quindos, A. Bonet, N. Diaz-Caneja, P. Fernandez, I. Gutierrez, J. Solana, J. Soto, E. Villar,
657 Study of the environmental variables affecting the natural preservation of the Altamira Cave
658 paintings located at Santillana del Mar, Spain, *Atmospheric Environment* (1967) 21 (1987)
659 551 – 560.
- 660 [2] S. Sánchez-Moral, V. Soler, J. Cañaveras, E. Sanz-Rubio, R. Van Grieken, K. Gysels, Inorganic
661 deterioration affecting the Altamira Cave, N Spain: quantitative approach to wall-corrosion
662 (solutional etching) processes induced by visitors, *Science of The Total Environment* 243-244
663 (1999) 67 – 84.
- 664 [3] D. Lacanette, S. Vincent, A. Sarthou, P. Malaurent, J.-P. Caltagirone, An Eulerian/Lagrangian
665 method for the numerical simulation of incompressible convection flows interacting with com-
666 plex obstacles: Application to the natural convection in the Lascaux cave, *Int. J. Heat Mass*
667 *Transfer* (2009) 2528–2542.
- 668 [4] P. Malaurent, J. Brunet, D. Lacanette, J.-P. Caltagirone, Contribution of numerical modelling
669 of environmental parameters to the conservation of prehistoric cave paintings: the example of
670 Lascaux cave, *Conservation and Management of Archaeological Sites* 8 (2007) 59–76.
- 671 [5] R. Ginet, Etude écologique de la grotte de la Balme, Isère, *Bull. biologique de la France et de*
672 *la Belgique* 85 (1951) 422–447.
- 673 [6] D. Culver, T. Pipan, *The biology of caves and other subterranean habitats*, Oxford University
674 Press, 2009.
- 675 [7] D. Sánchez-Fernández, V. Rizzo, A. Cieslak, A. Faille, J. Fresneda, I. Ribera, Thermal niche
676 estimators and the capability of poor dispersal species to cope with climate change, *Scientific*
677 *Reports* 6 (2016) 23381.
- 678 [8] P.-Y. Jeannin, A. Malard, D. Rickerl, E. Weber, Assessing karst-hydraulic hazards in
679 tunneling—the Brunnmühle spring system—Bernese Jura, Switzerland, *Environmental Earth*
680 *Sciences* 74 (2015) 7655–7670.
- 681 [9] A. Borsato, V. E. Johnston, S. Frisia, R. Miorandi, F. Corradini, Temperature and altitudinal
682 influence on karst dripwater chemistry: Implications for regional-scale palaeoclimate recon-
683 structions from speleothems, *Geochimica et Cosmochimica Acta* 177 (2016) 275–297.

- 684 [10] R. C. Casteel, J. L. Banner, Temperature-driven seasonal calcite growth and drip water trace
685 element variations in a well-ventilated Texas cave: Implications for speleothem paleoclimate
686 studies, *Chemical Geology* 392 (2015) 43–58.
- 687 [11] C. Andrieux, Contribution à l'étude du climat des cavités naturelles des massifs karstiques,
688 Ph.D. thesis, Université de Bordeaux, France, 1969.
- 689 [12] F. Bourges, P. Genthon, D. Genty, M. Lorblanchet, E. Mauduit, D. D'Hulst, Conservation of
690 prehistoric caves and stability of their inner climate: Lessons from Chauvet and other French
691 caves, *Science of The Total Environment* 493 (2014) 79 – 91.
- 692 [13] J. Brunet, J. Marsal, P. Vidal, Lascaux : où en sont les travaux de conservation ?, *Archéologia*
693 149 (1980).
- 694 [14] C. Andrieux, Etude des circulations d'air dans la grotte de Niaux: conséquences, *Karstologia*
695 1 (1983) 19–24.
- 696 [15] A. Al-Omari, X. Brunetaud, K. Beck, M. Al-Mukhtar, Effect of thermal stress, condensation
697 and freezing-thawing action on the degradation of stones on the Castle of Chambord, France,
698 *Environ Earth Sci* 71 (2014) 3977–3989.
- 699 [16] J.-B. Fourier, *Théorie analytique de la chaleur*, Gauthier-Villars, 1822.
- 700 [17] D. Domínguez-Villar, I. J. Fairchild, A. Baker, R. M. Carrasco, J. Pedraza, Reconstruction
701 of cave air temperature based on surface atmosphere temperature and vegetation changes:
702 Implications for speleothem palaeoclimate records, *Earth and Planetary Science Letters* 369–
703 370 (2013) 158 – 168.
- 704 [18] D. Domínguez-Villar, S. Lojen, K. Krklec, A. Baker, I. J. Fairchild, Is global warming affecting
705 cave temperatures? experimental and model data from a paradigmatic case study, *Climate*
706 *dynamics* 45 (2015) 569–581.
- 707 [19] H. S. Carslaw, J. C. Jaeger, *Conduction of Heat in Solids*, Oxford Clarendon Press, 1959.
- 708 [20] H. Schoeller, *La température des eaux souterraines*, Laboratoire de Géologie de la Faculté des
709 Sciences, Bordeaux, France, 1949.
- 710 [21] C. R. De Freitas, R. N. Littlejohn, Cave climate: Assessment of heat and moisture exchange,
711 *Journal of Climatology* 7 (1987) 553–569.

- 712 [22] C. De Freitas, A. Schmekal, Condensation as a microclimate process: measurement, numerical
713 simulation and prediction in the Glowworm Cave, New Zealand, *International Journal of*
714 *Climatology* 23 (2003) 557–575.
- 715 [23] C. De Freitas, S. Antje Anna, Studies of condensation/evaporation processes in the Glowworm
716 Cave, New Zealand, *International Journal of Speleology* 35 (2006).
- 717 [24] P. Malaurent, D. Lacanette, J. Brunet, J. Riss, Climatologie du milieu souterrain à lascaux:
718 d’une étude globale à la microclimatologie des parois, *Documents d’archéologie française* 105
719 (2011) 121–142.
- 720 [25] L. Laiz, J. Gonzalez, C. Saiz-Jimenez, Microbial communities in caves: ecology, physiology,
721 and effects on paleolithic paintings, *Art, biology, and conservation: Biodeterioration of works*
722 *of art* (2003) 210–225.
- 723 [26] National Research Council, Basic Research Opportunities in Earth Science, The National
724 Academies Press, Washington, DC, 2001.
- 725 [27] G. Badino, Underground drainage systems and geothermal flux, *Acta carsologica* 34 (2005).
- 726 [28] B. Lismonde, Climatologie du monde souterrain., Édition du Comité Départemental de
727 Spéléologie de l’Isère, Grenoble., 2002.
- 728 [29] M. Luetscher, P. Jeannin, Temperature distribution in karst systems: the role of air and water
729 fluxes, *Terra Nova* 16 (2004) 344–350.
- 730 [30] H. Schoeller, Étude géologique, hydrogéologique et climatologique de la grotte de lascaux
731 pendant le cycle 1964–1965, Rapport pour la première commission scientifique internationale
732 de la grotte de Lascaux, Université Bordeaux1, France, 97p (1965).
- 733 [31] J. Vouvé, J. Brunet, P. V. et, J. Marsal, Les oeuvres rupestres de Lascaux (Montignac, France):
734 maintien des conditions de conservation, *Studies in Conservation* 28 (1983) 107–116.
- 735 [32] E. Cussler, *Diffusion mass transfer in fluid systems*, Cambridge University Press, 1997.
- 736 [33] A. Adamson, *Physical Chemistry of Surfaces*, J. Wiley, 1990.
- 737 [34] F. P. Incropera, D. D. Dewitt, T. D. Bergman, A. S. Lavine, *Fundamentals of Heat and Mass*
738 *Transfer*, Wiley international edition, New York, 2007.
- 739 [35] E. Sparrow, R. Cess, *Radiation Heat Transfer*, McGraw–Hill Book Company, 1978.

- 740 [36] A. Bejan, Convection heat transfer, John Wiley and sons, 1995.
- 741 [37] J. Riddick, W. Bunger, T. Sakano, Organic Solvents: Physical Properties and Methods of
742 Purification, John Wiley and sons, 1986.
- 743 [38] R. W. Hyland, A. Wexler, Formulations for the thermodynamic properties of the saturated
744 phases of H₂O from 173.15 K to 473.15 K, ASHRAE transactions 89 (1983) 500–519.
- 745 [39] W. Rohsenow, J. Hartnett, Y. Cho, Handbook of Heat Transfer, McGraw-Hill, 1998.
- 746 [40] J. Smerdon, M. Stieglitz, Simulating heat transport of harmonic temperature signals in the
747 Earth’s shallow subsurface: Lower-boundary sensitivities, Geophysical Research Letters 33
748 (2006).
- 749 [41] N. Houillon, R. Lastennet, A. Denis, P. Malaurent, M. S., N. Peyraube, Assessing cave inter-
750 nal aerology in understanding carbon dioxide (CO₂) dynamics: implications on calcite mass
751 variation on the wall of Lascaux Cave (France), Environmental Earth Sciences 76:170 (2017).
- 752 [42] R. Buecher, Pre-development studies at Kartchner Caverns, in: National Cave Management
753 Symposium Proceedings, Bowling Green, Kentucky.
- 754 [43] N. Houillon, Inorganic carbon dynamics into the soil-epikarst-cavity continuum of the Lascaux
755 Cave (Dordogne, France), PhD Thesis, Université de Bordeaux, 2016.
- 756 [44] H. Beltrami, L. Kellman, An examination of short- and long-term air-ground temperature
757 coupling, Global and Planetary Change 38 (2003).
- 758 [45] Y. Li, D. Ogura, S. Hokoi, I. Takeshi, Effects of emergency preservation measures following
759 excavation of mural paintings in Takamatsuzuka Tumulus, Journal of Building Physics 36
760 (2012).
- 761 [46] Y. Li, D. Ogura, S. Hokoi, J. Wang, I. Takeshi, Predicting hygrothermal behaviors of the
762 underground stone chamber with 3-D modeling for restraining water-related damages on mural
763 paintings, Journal of Asian Architecture and Building Engineering 13 (2014).